IVYSPRING INTERNATIONAL PUBLISHER

JOURNAL OF CANCER

2026; 17(12): 2137-2153. doi: 10.7150/jca.141576

Research Paper

Integrative Multi-Cohort and Single-Cell Analyses Identify KIF11 as a Prognostic and Immune-Cold Marker in Lung Adenocarcinoma

Wenbin Jia[1,2,3,4#], Zewei Zhao[1,2,3,4#], Chunlan Ning[1,2,3,4#], Jiaqi Zhou[1,2,3,4], Bowen Liu[1,2,3,4], Xinchao Li[1,2,3,4], Yu Zou[1,2,3,4], Xuchen Cao[1,2,3,4], Xin Wang[1,2,3,4✉], Yue Yu[1,2,3,4✉]

1. The First Department of Breast Cancer, Tianjin Medical University Cancer Institute and Hospital, National Clinical Research Center for Cancer, Tianjin 300060, China.
2. Key Laboratory of Cancer Prevention and Therapy, Tianjin 300060, China.
3. Tianjin's Clinical Research Center for Cancer, Tianjin 300060, China.
4. Key Laboratory of Breast Cancer Prevention and Therapy, Tianjin Medical University, Ministry of Education, Tianjin 300060, China.

# These authors contributed equally to this work.

✉ Corresponding authors: Prof. Yue Yu, The First Department of Breast Cancer, Tianjin Medical University Cancer Institute and Hospital, Huan-Hu-Xi Road, He-Xi District, Tianjin 300060, China. E-mail: yuyue@tmu.edu.cn. Prof. Xin Wang, The First Department of Breast Cancer, Tianjin Medical University Cancer Institute and Hospital, Huan-Hu-Xi Road, He-Xi District, Tianjin 300060, China. E-mail: wangxin@tjmuch.com.

© 2026 The Author(s). This is an open access article distributed under the Creative Commons Attribution 4.0 International Licence, subject to the Publisher's Terms of Use at https://ivyspring.com/terms.

Received: 2026.07.27; Accepted: 2026.10.03; Published: 2026.11.13

Abstract

Lung adenocarcinoma (LUAD) is characterized by substantial molecular heterogeneity and marked differences in clinical outcome and therapeutic response. Although the mechanical microenvironment contributes to tumor progression and immune regulation, the prognostic and immunological relevance of mechanobiology-related genes in LUAD remains incompletely understood. In this study, we integrated transcriptomic, clinical, genomic, immunotherapy, and single-cell RNA-sequencing data to construct and validate a mechanobiology-related prognostic signature for LUAD. A machine-learning framework comprising 101 algorithmic combinations identified the StepCox[forward] plus Ridge model as the optimal prognostic model, which showed stable predictive performance across the TCGA training cohort and five independent validation cohorts. Subsequent screening identified KIF11, an intracellular mitotic kinesin involved in microtubule and spindle mechanics, as a core high-risk gene within the signature. Elevated KIF11 expression was associated with unfavorable overall survival, reduced stromal and immune scores, increased tumor purity, and an immune-cold tumor phenotype. In independent immune checkpoint blockade cohorts, KIF11 expression was higher in non-responders than in responders, while KIF11-high tumors exhibited higher TIDE scores and lower immunophenoscores, suggesting a reduced likelihood of benefit from immunotherapy. Single-cell analysis further localized the KIF11-associated phenotype to malignant epithelial cells, in which high KIF11 expression was accompanied by enrichment of E2F targets, G2/M checkpoint, MYC targets, and mitotic spindle programs, together with suppression of inflammatory-response and TNF-α/NF-κB signaling. Finally, KIF11 knockdown reduced cell viability, clonogenic growth, migration, and wound closure in H460 and H1299 lung cancer cells. Collectively, these findings establish a mechanobiology-related prognostic framework and identify the intracellular mitotic motor KIF11 as a candidate biomarker associated with aggressive tumor behavior, immune-cold features, and poor immunotherapy response in LUAD.

Keywords: lung adenocarcinoma; KIF11; mechanobiology; machine learning; prognostic signature; tumor immune microenvironment; immunotherapy

Introduction

Globally, lung cancer continues to rank among the principal causes of cancer-related death [1]. Lung adenocarcinoma (LUAD), the most prevalent histological form of non-small-cell lung cancer (NSCLC), provides an important disease setting for molecular classification and precision oncology [2].

More recently, progress in targeted therapy, immunotherapy, and multidisciplinary care has translated into better clinical outcomes for a subset of patients with LUAD. However, LUAD still exhibits substantial molecular and clinical heterogeneity, and patients differ markedly in disease progression, therapeutic sensitivity, and long-term prognosis. Therefore, identifying key molecules associated with LUAD progression and prognosis may help optimize patient stratification and provide new clues for potential therapeutic strategies.

In addition to genetic alterations and classical oncogenic signaling pathways, the physical and mechanical microenvironment of tumors has attracted increasing attention. Cells continuously sense extracellular matrix properties, neighboring cells, and physical stress, and convert mechanical forces into biochemical signals that regulate cellular and extracellular structures [3]. During tumor development and progression, tumor tissues often undergo extracellular matrix deposition, collagen fiber remodeling, increased tissue stiffness, altered cytoskeletal tension, and enhanced mechanical interactions between cells [4]. These mechanical factors can influence tumor cell proliferation, migration, invasion, and therapeutic resistance through cell adhesion, cytoskeletal remodeling, microtubule dynamics, and mechanotransduction signaling [5].

Concurrently, the mechanical microenvironment may help shape the tumor immune microenvironment through mechanisms that include modulation of immune-cell infiltration, migration, and functional states [6-8]. In particular, tumor-associated extracellular matrix remodeling can influence immune cell access and local immune regulation within tumor tissues [5]. Thus, analyzing LUAD from the perspective of mechanobiology-related molecules may provide a new angle for understanding tumor progression and immune microenvironmental heterogeneity.

Mechanobiology-related genes are not limited to extracellular matrix components or classical mechanotransduction molecules; they also include genes involved in cytoskeletal regulation, microtubule dynamics, spindle assembly, motor protein activity, and mitotic mechanics [9]. Together, these genes reflect the interaction between tumor cells and their physical microenvironment. If mechanobiology-related molecules are linked to both patient prognosis and immune microenvironmental status, they may have value as risk markers and potentially contribute to malignant phenotypes in LUAD.

In this study, we systematically analyzed LUAD transcriptomic and clinical data based on a mechanobiology-related gene set and constructed a mechanobiology-related prognostic model. Through multi-cohort validation and core gene screening, we identified KIF11 as one of the important candidate molecules in the model. KIF11, alternatively termed Eg5 or kinesin family member 11, is an ATP-dependent microtubule motor protein that primarily supports mitotic spindle assembly, maintenance, and bipolar organization [10]. By regulating microtubule sliding and spindle mechanical balance, KIF11 contributes to proper chromosome segregation and cell-cycle progression [11]. Although KIF11 is not a canonical mechanosensor of extracellular-matrix stiffness, its established roles in microtubule sliding, spindle organization, and mitotic force generation place it within the broader framework of intracellular mechanobiology. Accordingly, in the present study, KIF11 is considered a mechanobiology-related intracellular motor rather than a direct mediator of extracellular mechanical signaling.

Earlier work has largely examined the fundamental functions of microtubule motor proteins in cell-cycle progression and mitotic control. However, the links between KIF11 and mechanobiology-related transcriptional features, prognostic risk, and the immune microenvironment in LUAD remain poorly defined. Our analysis linked elevated KIF11 expression to poorer prognosis and a trend toward lower immune infiltration. These findings suggest that KIF11-high tumors may represent a LUAD state marked by heightened microtubule dynamics, increased mitotic activity, and altered immune microenvironmental features. Accordingly, this study examines the potential relevance of KIF11 in LUAD from a mechanobiological perspective. The findings may inform LUAD risk stratification, immune microenvironment research, and subsequent mechanistic investigations.

Methods

Multi-source data integration

The primary training dataset from The Cancer Genome Atlas (TCGA) portal comprised transcriptomic, clinical, copy-number variation, and somatic mutation data for patients with lung adenocarcinoma (LUAD). The TCGA cohort was used for machine-learning model training (dataset 1), whereas five independent transcriptomic datasets were included for external validation: GSE31210 (dataset 2), GSE72094 (dataset 3), GSE68465 (dataset 4), GSE13213 (dataset 5), and GSE26939 (dataset 6). To further evaluate differences in immunotherapy responsiveness, three independent immunotherapy datasets, GSE126044, GSE166449, and GSE207422 [12-

14], were integrated. Single-cell RNA sequencing analysis used the GSE131907 dataset [15], consisting of 11 primary early-stage LUAD samples and four advanced-stage LUAD samples. Mechanobiology-related genes (MRGs) were compiled through a systematic and comprehensive literature search. Data integration involved transcripts-per-million normalization, batch-effect correction with the ComBat function in the sva R package, and logarithmic transformation. Principal component analysis (PCA) was subsequently applied to assess residual batch effects. The complete MRGs list is provided in Supplementary Table 1.

Identification of mechanobiology-related prognostic genes and signatures

Gene expression profiles from LUAD tumors and normal tissues were compared using the limma R package [16]. Genes meeting the thresholds of $|\log FC| > 1$ and adjusted P value < 0.05 were classified as differentially expressed. The resulting genes were cross-referenced with the MRGs set, and shared candidates were assessed by univariate Cox regression for prognostic associations. The Mime1 R package was used to integrate 10 machine-learning algorithms and 101 algorithmic combinations for the construction of candidate prognostic models. The mean concordance index (C-index) across the validation cohorts served as the primary criterion for selecting the model-feature combination with the strongest overall predictive performance. Model discrimination was further examined through receiver operating characteristic (ROC) analysis and principal component analysis (PCA). The proposed model was also systematically compared with contemporary LUAD prognostic models to contextualize its performance relative to existing research. The prognostic utility of the model was further assessed by Kaplan–Meier survival analysis.

Genomic alteration and immune landscape analyses

Genomic alterations were analyzed using GISTIC 2.0, with particular attention given to recurrent genomic amplifications and deletions. The maftools R package was used for visualization. To further characterize the association between the key genes identified from the MRPs and the immune landscape, as well as to identify patients who might benefit from immunotherapy, the ESTIMATE R package was used to infer the relative proportions of immune and stromal components in tumor tissues from transcriptomic data and to calculate tumor purity [17]. We evaluated the potential response to immunotherapy associated with KIF11 and determined TIDE scores using the Tumor Immune Dysfunction and Exclusion (TIDE) algorithm (http://tide.dfci.harvard.edu/). Additionally, immunophenoscores were retrieved from The Cancer Immunome Atlas database (TCIA; https://tcia.at/home).

Mechanistic and pathway analyses

The R package clusterProfiler was executed to conduct Gene Ontology (GO) annotation and Kyoto Encyclopedia of Genes and Genomes (KEGG) pathway enrichment analyses for the identified core genes [18]. Gene symbols were first converted into Entrez Gene identifiers based on the org.Hs.eg.db annotation database. The enrichGO function was subsequently used to evaluate biological processes, cellular components, and molecular functions, whereas the enrichKEGG function was used to conduct human KEGG pathway enrichment analysis. In the resulting bar charts, the size of each bar reflected the count of genes assigned to the respective pathway or functional term. We retrieved human Hallmark gene sets from the Molecular Signatures Database (MSigDB) via the R package msigdbr, subsequently executing gene set enrichment analysis (GSEA) with clusterProfiler. A normalized enrichment score (NES) > 0 indicated that the corresponding pathway tended to be enriched in KIF11-positive malignant cells, whereas a NES < 0 indicated preferential enrichment in KIF11-negative malignant cells. Ridge plots and GSEA enrichment curves for representative pathways were conducted using the enrichplot R package.

Single-cell RNA sequencing data preprocessing

Single-cell transcriptomic datasets were processed using the Seurat R package. To maintain rigorous data quality, standard filtering steps were implemented. Specifically, single cells were selected based on defined thresholds: nFeature_RNA ≥ 200, nCount_RNA ≥ 100, log10FeaturePerUMI ≥ 0.8, percent_mito ≤ 20, and percent_hb ≤ 3. Putative doublets were then detected and excluded via the DoubletFinder package [19]. Heterogeneous samples from different sources were integrated using Harmony, which was also used to correct intersample batch effects [20]. Finally, SCTransform was applied for data normalization and to reduce variation attributable to technical factors [21]. The inferCNV package was employed to compare gene expression intensity between epithelial cells and reference myeloid cells, identifying differences in large-scale somatic chromosomal copy number variations thereby revealing alterations in malignant epithelial cells.

Cell culture

We purchased the human bronchial epithelial cell line (BEAS-2B) and human lung cancer cell lines (A549, H1299, H460, H1975, and PC9) from the Cell Bank of the Chinese Academy of Sciences (Shanghai, China). Culture media consisted of Dulbecco's modified Eagle's medium (DMEM; Gibco) supplemented with 10% fetal bovine serum (FBS; Gibco) and 1% penicillin-streptomycin mixture (Gibco, USA). All cell cultures were maintained in a humidified 37°C atmosphere with 5% CO_2.

siRNA transfection

Three independent small interfering RNAs targeting distinct regions of the human KIF11 coding sequence, designated si-KIF11 1#, si-KIF11 2#, and si-KIF11 3#, were designed and synthesized by GenePharma (Shanghai, China). A scrambled siRNA with no known homology to human transcripts was used as the negative control (si-NC). The siRNA sequences are as follows:

si-KIF11 1#: ACAUUCUACUAUUGAAUGGGC, CCAUUCAAUAGUAGAAUGUGA;

si-KIF11 2#: AAACCUUUAAUUAUCACUCCU, GAGUGAUAAUUAAAGGUUUAG;

si-KIF11 3#: AAACAACACUUCGGUAAACAU, GUUUACCGAAGUGUUGUUUGU.

H460 and H1299 cells were seeded in six-well plates at a density of $2x10^5$ cells per well and cultured until they reached approximately 70–80% confluence. Cells were transfected with the indicated siRNAs at a final concentration of 50 nM using Lipofectamine 3000 reagent (Invitrogen, Carlsbad, CA, USA), according to the manufacturer's instructions. Cells were harvested 48 h after transfection to evaluate knockdown efficiency and were subsequently used for the functional assays. Based on the qRT-PCR results, si-KIF11 1# and si-KIF11 2# were selected for subsequent functional experiments and further protein-level validation by Western blotting.

RNA extraction and quantitative real-time PCR

We isolated total RNA using the RNAiso Plus reagent (Takara, Beijing, China) following the manufacturer's guidelines. Subsequently, RNA concentrations were quantified with a NanoOne ultra-micro volume spectrophotometer (Hangzhou Yooning Instruments Co., Ltd., Hangzhou, China). RNA was reverse-transcribed into complementary DNA using the HiScript III 1st Strand cDNA Synthesis Kit with genomic DNA removal. Quantitative real-time PCR was performed using a LightCycler 480 Instrument II real-time PCR system. GAPDH was used as the internal reference gene. Relative KIF11 expression was calculated using the ($2^{-\Delta\Delta Ct}$) method. For comparisons among cell lines, BEAS-2B cells were used as the calibrator. For assessment of siRNA-mediated knockdown, the corresponding si-NC group was used as the calibrator. The GAPDH primer sequences are as follows: forward, 5′-GGAGCGAGATCCCTCCAAAAT-3′; and reverse, 5′-GGCTGTTGTCATACTTCTCATGG-3′. The KIF11 primer sequences are as follows: forward, 5′-GCTTTCTCCTCGGCTCACTT-3′; and reverse, 5′-GTGGGCACAGAGCCATTAGT-3′.

Cell viability assay

The Cell Counting Kit-8 (CCK-8; Dojindo Laboratories, Kumamoto, Japan) was employed to determine cellular viability. Following 48 h of siRNA transfection, H460 and H1299 cells were collected and plated into 96-well plates (2 × 10^3 cells/well) with three replicate wells per condition. At 0, 24, 48, 72, and 96 h, 10 µL of CCK-8 reagent was introduced to each well. After incubating for 2 h at 37°C, absorbance values were detected at 450 nm via a Varioskan LUX multimode microplate reader (Thermo Fisher Scientific, Waltham, MA, USA).

Colony-formation assay

To measure clonogenic survival, transfected H460 and H1299 cells (48 h post-transfection) were plated into six-well plates (800 cells/well, in triplicate) and cultured in complete medium for 10 days, with fluid replacement occurring every 3 days. Afterwards, PBS-washed cell colonies were fixed using 4% paraformaldehyde for 15 min and stained with 0.1% crystal violet for 20 min at ambient temperature. Once residual stain was rinsed away, visible colonies (>50 cells/colony) were enumerated under an inverted light microscope.

Transwell migration assay

Cell migration was evaluated using 24-well Transwell chambers fitted with polycarbonate membranes with an 8-µm pore size (Corning Inc., Corning, NY, USA). At 48 h after transfection, ($1×10^5$) H460 or H1299 cells were resuspended in serum-free DMEM and added to the upper chamber. To induce cell migration, 600 µL of DMEM supplemented with 10% FBS was placed into the lower wells. Following a 24-h incubation period at 37°C, residual cells on the top membrane surface were gently cleared using a cotton swab. Cells that successfully migrated through the membrane were fixed with 4% paraformaldehyde (15 min) and stained using 0.1% crystal violet (20 min). Stained membranes were subsequently photographed under an inverted microscope at ×200 magnification.

Migrated cells were counted in five randomly selected microscopic fields per membrane. Three independent Transwell chambers were evaluated for each experimental group, and the mean count from the five fields was used as the value for each chamber.

Wound-healing assay

H460 and H1299 cells were seeded into six-well plates after siRNA transfection and cultured until a confluent monolayer was formed. A straight scratch was created across the confluent cell monolayer using a sterile pipette tip. After washing the wells with PBS to remove cellular debris, fresh serum-free DMEM was added to minimize the contribution of cell proliferation during the migration assay. Wound closure was monitored at 0 and 24 h post-wounding, and representative fields were photographed using an inverted microscope.

Western blot analysis

Total cellular protein was extracted using RIPA lysis buffer supplemented with 1% phenylmethylsulfonyl fluoride (PMSF) and protease inhibitor cocktail. Cells were lysed on ice for 30 min, followed by centrifugation at 12,000 × g for 15 min at 4°C to collect the supernatant. Protein concentration was determined using the BCA Protein Assay Kit according to the manufacturer's instructions. Equal amounts of protein samples were separated by 10% sodium dodecyl sulfate-polyacrylamide gel electrophoresis (SDS-PAGE) and then electrophoretically transferred onto polyvinylidene difluoride (PVDF) membranes. After blocking with 5% non-fat milk in Tris-buffered saline containing 0.1% Tween-20 (TBST) for 1 h at room temperature, the membranes were incubated with primary antibodies overnight at 4°C. The primary antibodies used were as follows: anti-KIF11/Eg5 (Proteintech, Wuhan, China; Cat. No. 23333-1-AP; 1:2,000) and anti-GAPDH (Proteintech, Wuhan, China; Cat. No. 10494-1-AP; 1:10,000). After three washes with TBST, the membranes were incubated with horseradish peroxidase (HRP)-conjugated secondary antibody (Proteintech, Wuhan, China) for 1 h at room temperature. Protein bands were visualized using an enhanced chemiluminescence (ECL) (Thermo Fisher, USA) detection system. Band intensities were quantified using ImageJ software. KIF11 protein abundance was normalized to the corresponding GAPDH signal, and the normalized values were expressed relative to the si-NC group. Densitometric quantification was performed using three independent biological experiments.

Statistical analysis

Continuous data are presented as the mean ± standard deviation. Comparisons of KIF11 expression between BEAS-2B cells and individual lung cancer cell lines were performed using one-way analysis of variance followed by Dunnett's multiple-comparison test, with BEAS-2B as the reference group. The mRNA silencing efficiencies of the three KIF11-targeting siRNAs were evaluated using one-way ANOVA followed by Dunnett's multiple-comparison test, with si-NC as the reference group. Densitometric measurements of KIF11 protein expression for the two selected siRNAs were analyzed separately in H460 and H1299 cells using one-way ANOVA followed by Dunnett's multiple-comparison test, with si-NC as the reference group. CCK-8 measurements were analyzed using two-way analysis of variance, with treatment group and time as the two factors, followed by multiplicity-adjusted comparisons between each KIF11-knockdown group and the si-NC group. We analyzed quantitative data from colony-formation, Transwell migration, and wound-healing assays using one-way ANOVA with Dunnett's multiple-comparison test. All statistical evaluations were two-tailed. $P < 0.05$ was considered statistically significant (*$P < 0.05$, **$P < 0.01$, ***$P < 0.001$, and ****$P < 0.0001$). Data processing and statistical testing were performed using GraphPad Prism software (version 9.0; GraphPad Software, San Diego, CA, USA). Other statistical analyses were performed using R software (version 4.3.3).

Results

Landscape of transcriptomic DEGs, functional enrichment, and genomic alterations in LUAD

To systematically identify key oncogenic drivers in lung adenocarcinoma (LUAD), we first performed differential expression analysis between tumor and adjacent normal tissues. A series of significant differentially expressed genes (DEGs) were identified. By intersecting these with a mechanobiology-related gene set, we ultimately obtained 49 statistically significant, prognosis-related DEGs, which were distinctly clustered into two major modules (Figure 1A). The results revealed that numerous genes, including ANLN, RHOV, PLK1, and KIF11, acted as significant risk factors (hazard ratio [HR] > 1), whereas some downregulated genes exerted a protective prognostic effect (Figure 1B). Functional annotation through Gene Ontology (GO) and KEGG pathway analyses revealed that these DEGs were mainly involved in cell cycle regulation and structural remodeling. Specifically, Biological Processes (BP) were tightly linked to nuclear division and spindle

assembly; Cellular Components (CC) were concentrated on the microtubule, spindle, and midbody; and Molecular Functions (MF) focused on tubulin binding and cytoskeletal motor activity (Figure 1C). Concurrently, KEGG enrichment highlighted motor proteins and the relaxin signaling pathway (Figure 1C). Circular stacked bar plots further substantiated that these genes predominantly modulated extracellular matrix (ECM) organization, actin filament-based movement, and Hippo signaling (Figure 1D). At the genomic level, we mapped the chromosomal distribution and frequency of copy number variations (CNVs) across the human genome (Figure 1E, F). Significant copy number amplifications (AMP) were highly prevalent on chromosomes 1, 2, 6, and 7, while marked deletions (DEL) were preferentially clustered on chromosomes 3, 9, and 15, cross-validating the profound transcriptomic dysregulation driven by genomic instability in LUAD.

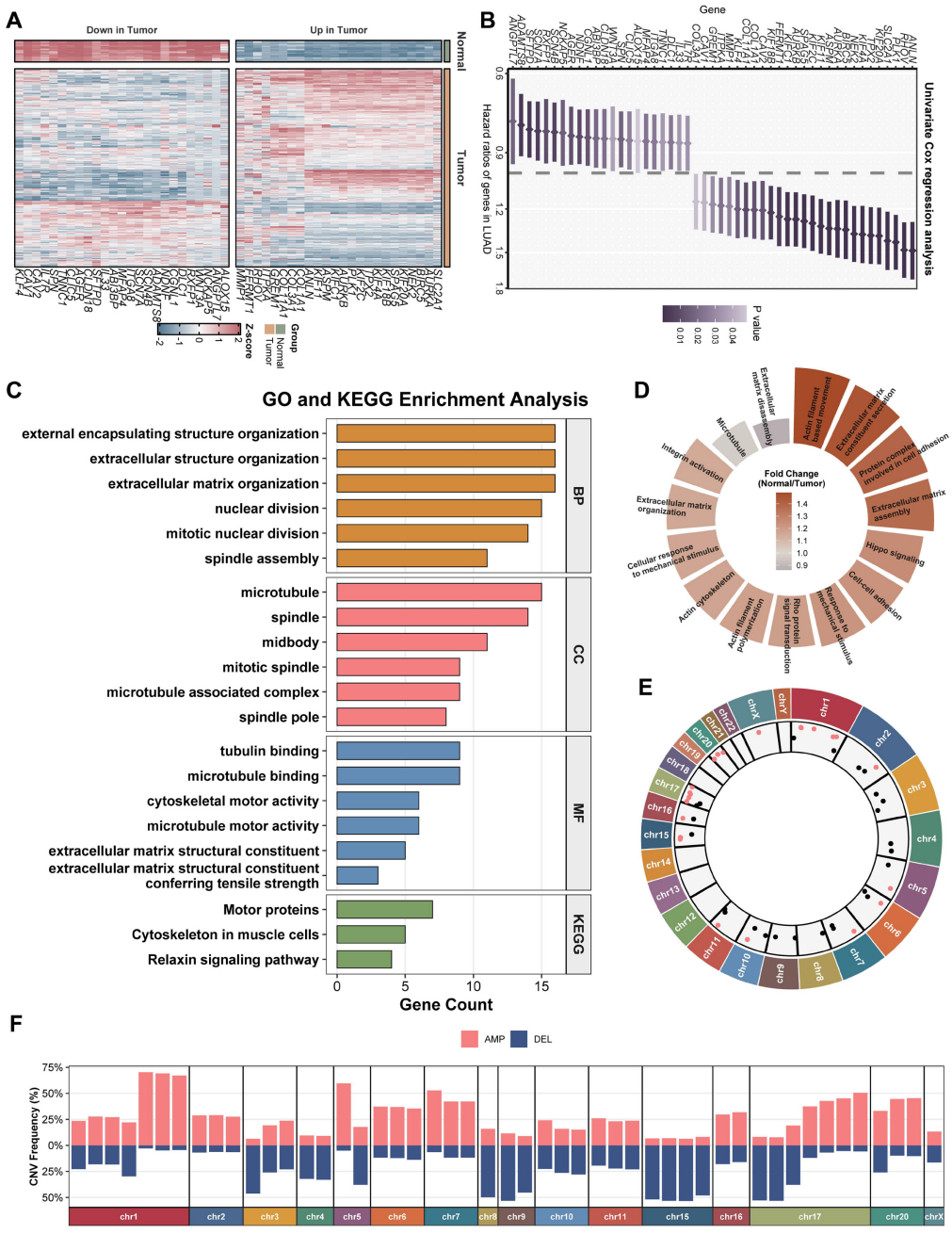


Figure 1. Landscape of mechanobiology-related prognostic genes, functional enrichment and genomic alterations in LUAD. (A) Heatmap showing expression patterns of prognosis-related mechanobiology-related differentially expressed genes (DEGs) in normal and LUAD tumor tissues. (B) Univariate Cox regression analysis of the identified genes; hazard ratios and 95% confidence intervals are shown. (C) Gene Ontology (GO) and Kyoto Encyclopedia of Genes and Genomes (KEGG) enrichment analyses of the DEGs. (D) Circular plot summarizing mechanical force- and cytoskeleton-related functional terms and their fold changes between normal and tumor tissue. (E) Genomic distribution of mechanobiology-related prognostic genes was mapped, with red indicators signifying elevated expression in neoplastic tissue (log2(FC) values correlate with radial position), while black indicators denote the inverse pattern. (F) Frequencies of copy-number amplification (AMP) and deletion (DEL) across chromosomes. LUAD, lung adenocarcinoma.

Development and cross-cohort validation of a machine learning-derived mechanobiology-related prognostic signature (MRPs)

To construct a highly robust and clinically applicable prognostic tool, we integrated multiple independent LUAD cohorts (dataset1 to dataset6) and implemented a consensus-based machine learning benchmarking pipeline comprising 101 algorithm combinations. Principal component analysis (PCA) showed substantially reduced cohort-associated separation after batch-effect correction, suggesting that major inter-cohort technical variation was mitigated (Figure 2C, D). Ultimately, the "StepCox[forward] + Ridge" combination emerged as the optimal algorithmic framework, achieving the most stable and highest mean Concordance Index (C-index) across both the training and validation cohorts (Figure 2A, B). Specifically, its mean C-index reached up to 0.657, verifying its reliable accuracy (Figure 2B). Utilizing the risk score formula derived from this model, patients across the six datasets were stratified into high-risk and low-risk groups. Kaplan-Meier survival analysis demonstrated statistically significant survival differences between the high- and low-risk groups in datasets 1-5, whereas dataset 6 showed a consistent trend toward poorer overall survival in the high-risk group that did not reach conventional statistical significance (HR = 1.60, P = 0.056).

Evaluation of model superiority and robustness

To further evaluate the prognostic performance of the MRPs, we compared its C-index with those of individual conventional clinical variables, including age, sex, smoking status, and tumor stage. Across the evaluated cohorts, the MRPs generally showed favorable discriminative performance relative to these individual clinical variables (Figure 3A). Across all tested cohorts, the C-index of our risk score outperformed standard clinical features such as age, gender, smoking, and even tumor stage. To further explore the molecular heterogeneity captured by the model, we projected the expression profiles of the model genes via PCA. Across all six cohorts, patients belonging to the high- and low-risk phenotypes presented clear spatial separation and distinct clustering patterns (Figure 3B–G). Notably, when benchmarking our prognostic model against dozens of previously published gene signatures, our signature consistently ranked among the top or at the absolute forefront in terms of C-index accuracy (Figure 3H). This rigorous cross-signature benchmarking establishes our signature as an outstanding prognostic framework for LUAD.

Identification of KIF11 as a core prognostic gene associated with the tumor microenvironment

To determine the predictive accuracy and identify the core driving components within our signature, we first calculated time-dependent ROC curves. The model exhibited high AUC (Area Under the Curve) values for 1-year (Figure 4A), 3-year (Figure 4B), and 5-year (Figure 4C) survival predictions, with the 1-year AUC reaching up to 0.879 in dataset5. Next, we extracted the selection frequency of each constituent gene during the machine learning screening pipeline. Among the top 20 core genes, PLK1, KIFC1, KIF20A, IL7R, and KIF11 exhibited the highest occurrence frequencies, underscoring their core indispensability (Figure 4D). Univariate Cox regression analysis re-confirmed that KIF11 is a profoundly strong and statistically significant risk factor in LUAD (Figure 4E). Concurrently, compared to the normal control group, KIF11 was expressed at significantly higher levels in LUAD tumor tissues ($P < 0.05$, Figure 4F). Within the present mechanobiology-related framework, KIF11 is interpreted as an intracellular mitotic kinesin associated with microtubule and spindle mechanics rather than as a direct sensor of extracellular matrix stiffness or tissue-level mechanical cues. Furthermore, we deeply analyzed the relationship between KIF11 and the tumor microenvironment (TME). Spearman correlation analysis revealed weak but statistically significant negative correlations between KIF11 expression and StromalScore ($R = -0.16$, $P = 0.00036$), ImmuneScore ($R = -0.16$, $P = 0.00033$), and ESTIMATEScore ($R = -0.17$, $P = 0.00015$), together with a weak positive correlation with estimated tumor purity ($R = 0.17$, $P = 0.00015$; Figure 4G–J). Although the effect sizes were modest, these associations indicate that higher KIF11 expression tended to occur in tumors with lower inferred stromal and immune content and higher estimated tumor purity.

KIF11 expression is associated with an immune-cold microenvironment and reduced immunotherapy responsiveness

Given its correlation with tumor purity and low immune infiltration, we further investigated the potential role of KIF11 in therapeutic resistance. First, we confirmed that KIF11 expression was strongly and positively correlated with the overall MRPs ($R = 0.77$, $P < 2.2e-16$; Figure 5A), and its expression was significantly upregulated in the high-risk patient group (Figure 5B). TCGA-based Kaplan-Meier survival analysis confirmed that, compared to the low KIF11 group, patients in the high KIF11 level group experienced significantly shortened overall survival

(log-rank P = 0.00048, HR = 1.7; Figure 5C). More importantly, in the integrated cohort receiving immune checkpoint blockade (ICB) therapy, KIF11 expression was higher in Non-Responders (NR) than in Responders (R) (P = 0.0081; Figure 5D). Subsequently, we utilized the TIDE algorithm. High KIF11 tumors exhibited significantly elevated TIDE scores (P < 0.0001; Figure 5E, F), implying a higher potential for local immune escape and T-cell exclusion. Chi-square analysis of TIDE-predicted response status showed a higher proportion of predicted non-responders in the KIF11-high group (Figure 5G, H). Additionally, evaluation of the Immunophenoscore (IPS) demonstrated that the high KIF11 group displayed significantly lower IPS scores across multiple treatment regimens, including CTLA4_neg/PD1_neg, CTLA4_pos/PD1_neg and CTLA4_neg/PD1_pos (Figure 5I). Collectively, these findings indicate that higher KIF11 expression is associated with an immune-cold tumor phenotype and reduced responsiveness to immune checkpoint blockade, supporting its potential utility as a candidate biomarker for immunotherapy stratification.

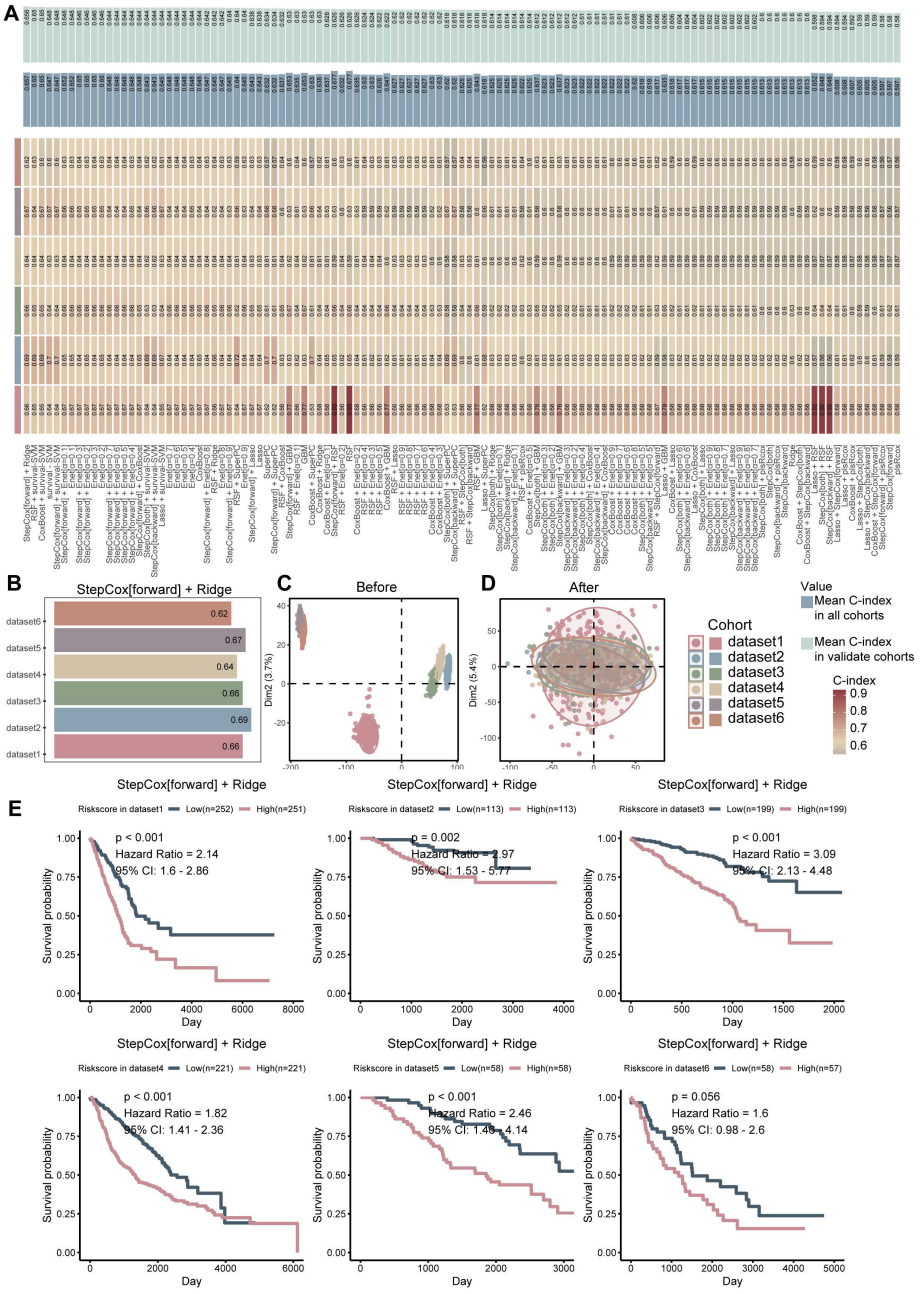


Figure 2. Construction and external validation of the mechanobiology-related prognostic signature (MRPs). (A) Heatmap of concordance indices (C-indices) for 101 machine-learning algorithm combinations across the training and validation cohorts. (B) C-index of the selected StepCox[forward] + Ridge model in each cohort. (C,D) Principal-component analysis before and after batch-effect correction, respectively. (E) Kaplan-Meier curves for overall survival in high- and low-risk groups across dataset1-dataset6. Hazard ratios and log-rank P values are displayed.

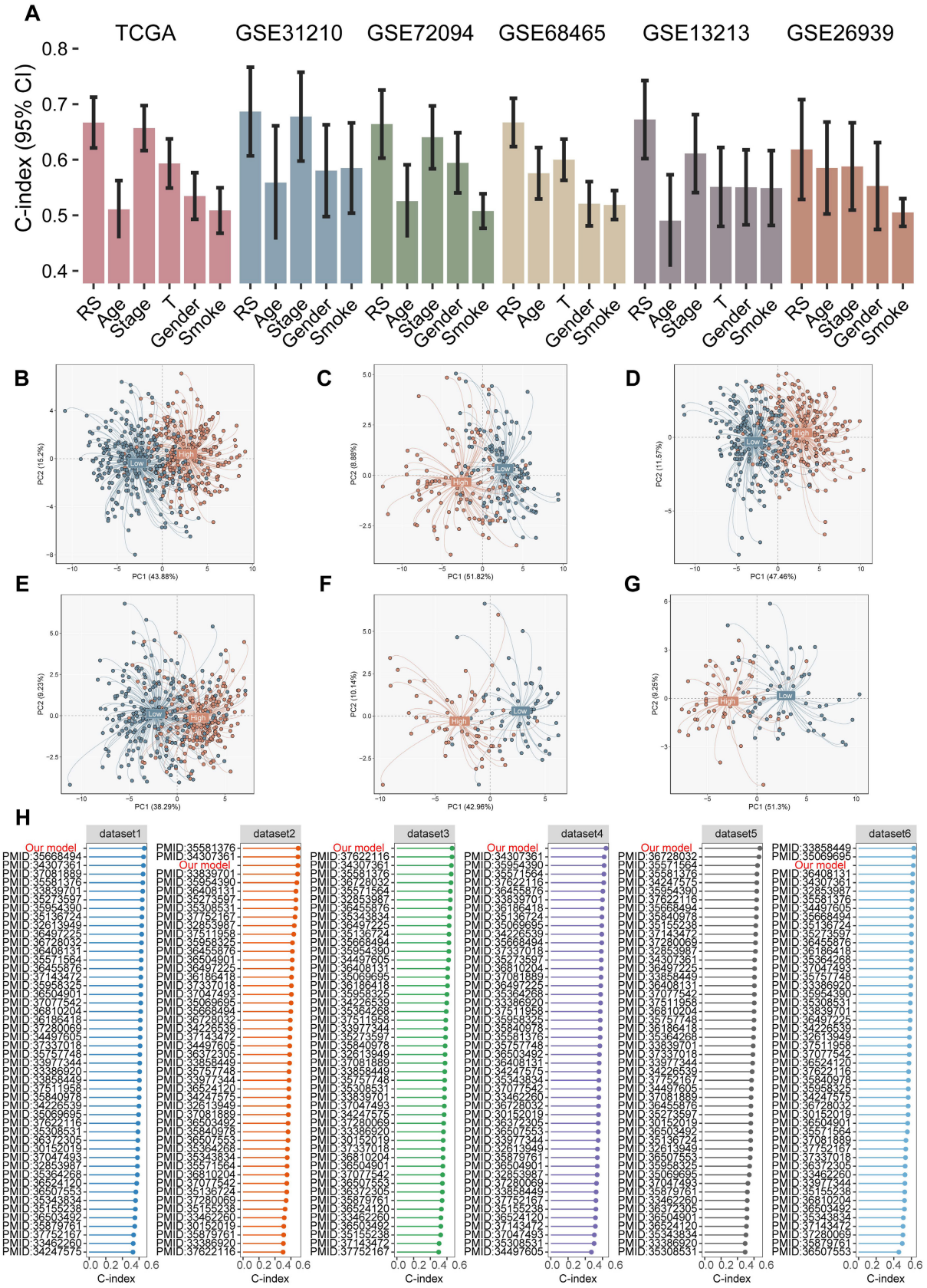


Figure 3. Assessment of MRPs performance and robustness across cohorts. (A) Comparison of C-indices for the MRPs risk score (RS) and conventional clinical variables in TCGA and five external cohorts. Error bars indicate 95% confidence intervals. (B-G) Principal-component analysis showing separation of low- and high-risk groups in dataset1-dataset6, respectively. (H) Benchmark comparison of C-indices between the present model and previously published LUAD prognostic signatures in each cohort.

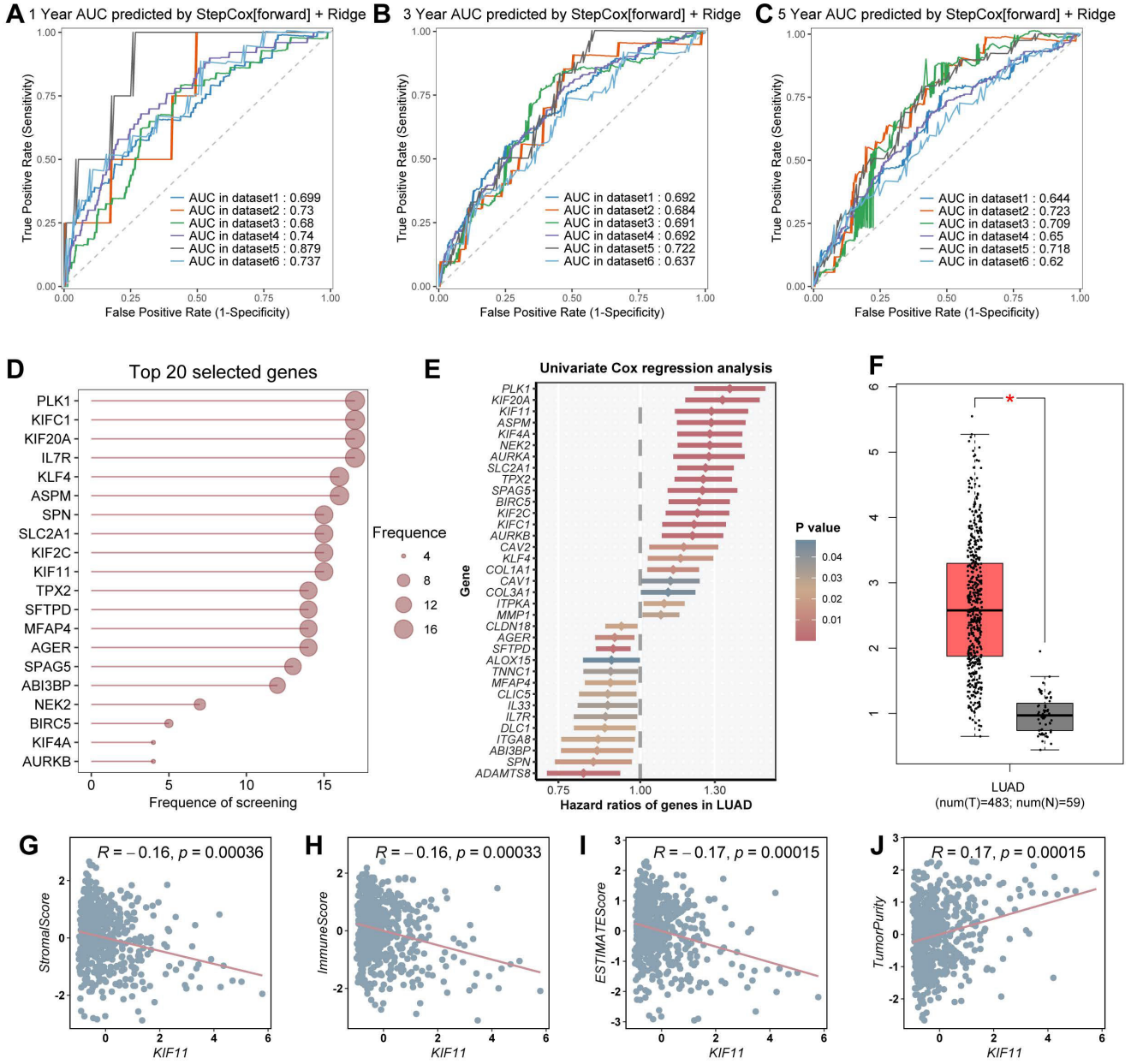


Figure 4. Identification of KIF11 as a core prognostic gene associated with the tumor microenvironment. (A-C) Time-dependent receiver-operating-characteristic curves for 1-, 3- and 5-year survival prediction by the StepCox[forward] + Ridge model across the six cohorts. (D) Frequencies with which the top 20 genes were selected in the machine-learning pipeline. (E) Univariate Cox regression analysis of selected core genes in LUAD. (F) KIF11 expression in LUAD tumor and normal tissues. (G-J) Correlations between KIF11 expression and StromalScore, ImmuneScore, ESTIMATEScore and estimated tumor purity, respectively. Correlations were assessed by Spearman analysis.

Hyper-proliferative and immune-evasive pathways highly enriched in KIF11-high malignant cells

To explore the biological characteristics of KIF11-high malignant epithelial tumor cells at single-cell resolution, we analyzed a scRNA-seq dataset of LUAD. Unsupervised clustering visualized by t-SNE (Figure 6A) and UMAP (Figure 6B) identified eight major distinct cell lineages: Epithelial cells, T cells, Myeloid cells, B cells, Fibroblasts, Plasma cells, Endothelial cells and Mast cells. To confirm the accuracy of the lineage definitions, we mapped the expression of lineage-specific marker genes via a dot plot (Figure 6C). Because the epithelial cell population contains both benign and malignant cells, we executed a large-scale InferCNV analysis to calculate chromosomal copy number profiles, using myeloid cells as the normal reference background (Figure 6D, E). We successfully identified a malignant epithelial cell subpopulation characterized by high-density clustering and extensive chromosomal aberrations

(Figure 6D, E). To characterize the transcriptional programs associated with KIF11 expression within these identified malignant cells, we stratified the malignant epithelial cell population into KIF11-high and KIF11-low subpopulations and performed GSEA analysis. Ridge plot visualizations of the Hallmark pathways demonstrated that KIF11-high malignant cells exhibited highly significant hyper-proliferation and activation of cell cycle-promoting networks, including E2F_TARGETS, G2M_CHECKPOINT, and MYC_TARGETS_V1 (Figure 7A). Conversely, pathways crucial to inflammatory signaling and immune cell chemotaxis, such as TNFA_SIGNALING_VIA_NFKB, INFLAMMATORY_RESPONSE, and the P53_PATHWAY were severely suppressed in the KIF11-high malignant phenotype (Figure 7A). Detailed GSEA running score plots further validated the trends of these specific pathways (Figure 7B, C, D). These single-cell transcriptomic findings indicate that KIF11-high malignant cells are characterized by enhanced proliferation-related programs together with reduced inflammatory signaling. This transcriptional state is consistent with the immune-cold features observed in the bulk-tissue analyses.

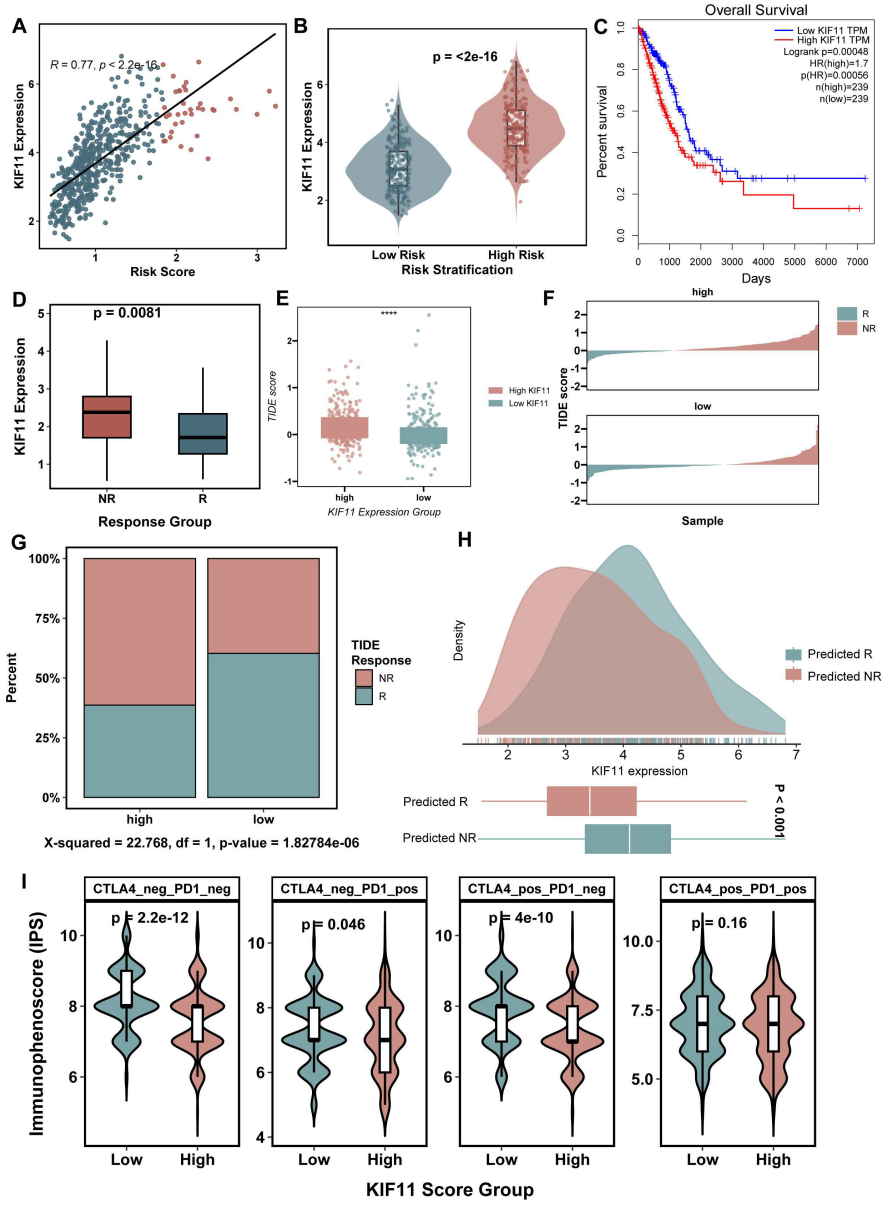


Figure 5. Association of KIF11 with risk stratification, ICB response-related metrics. (A) Correlation between KIF11 expression and MRPs risk score in the TCGA-LUAD cohort. (B) KIF11 expression in low- and high-risk groups. (C) Kaplan-Meier analysis of overall survival according to KIF11 expression. (D) KIF11 expression in responders (R) and non-responders (NR) in the integrated NSCLC-related ICB cohorts. (E) TIDE scores in KIF11-high and KIF11-low groups. (F) Distribution of TIDE scores and predicted response status in the KIF11-high and KIF11-low groups. (G) Proportions of TIDE-predicted responders and non-responders in the KIF11-high and KIF11-low groups in the TCGA-LUAD cohort. (H) Density distribution of KIF11 expression according to TIDE-predicted response status in the TCGA-LUAD cohort. (I) Immunophenoscores under the indicated CTLA4 and PD1 status combinations. ICB, immune checkpoint blockade; IPS, immunophenoscore; TIDE, Tumor Immune Dysfunction and Exclusion.

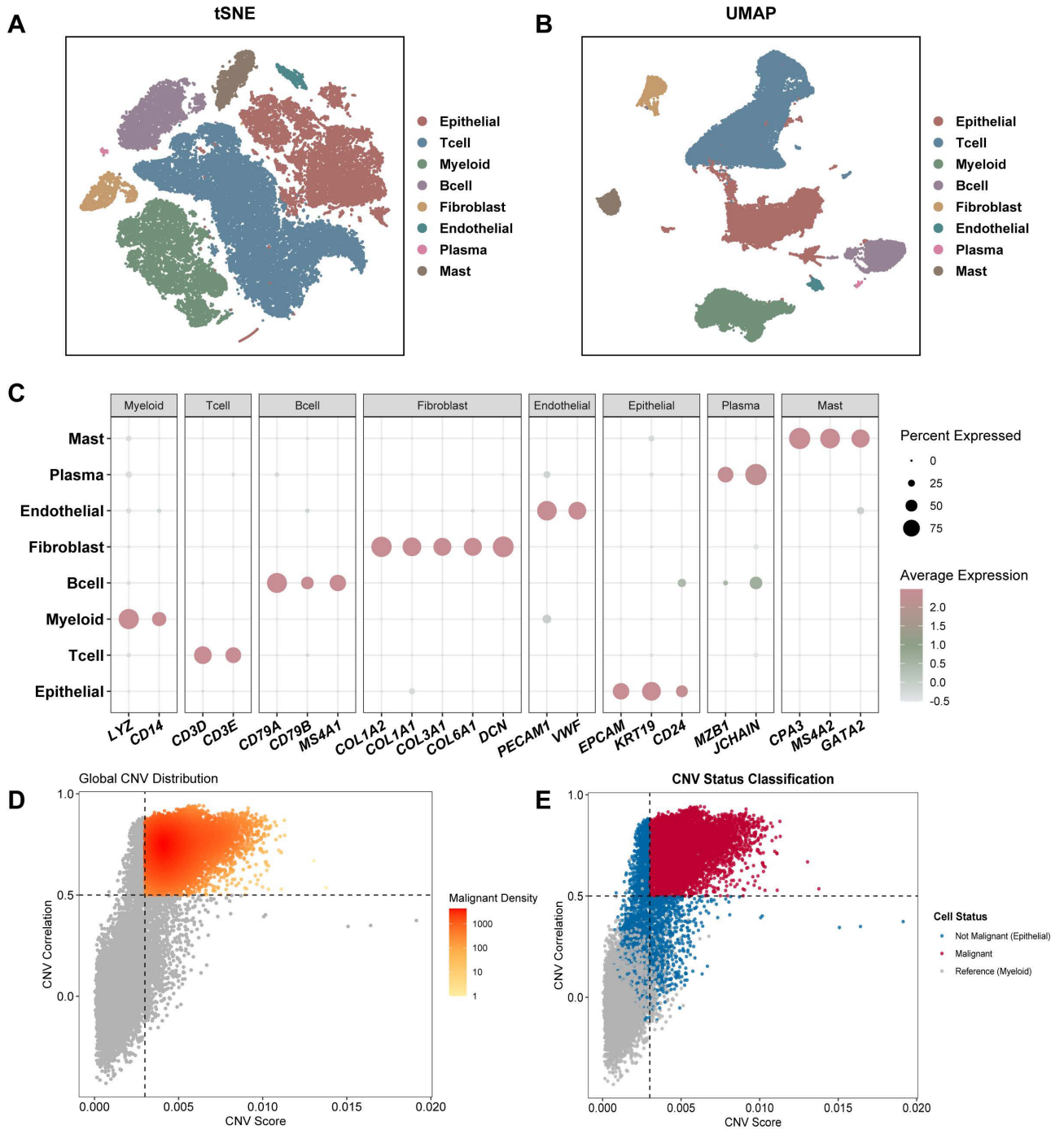


Figure 6. Single-cell identification of malignant epithelial cells in LUAD. (A,B) t-distributed stochastic neighbor embedding (t-SNE) and uniform manifold approximation and projection (UMAP) of major cell lineages in the GSE131907 LUAD single-cell dataset. (C) Dot plot of canonical marker genes used for cell-lineage annotation. Dot size indicates the percentage of cells expressing each gene and color indicates average expression. (D) Global copy-number-variation (CNV) distribution inferred from epithelial cells using myeloid cells as the reference population. (E) Classification of epithelial cells as malignant or non-malignant according to inferred CNV profiles.

KIF11 knockdown impairs the proliferative and migratory properties of lung cancer cells

We first examined KIF11 mRNA expression in the human bronchial epithelial cell line BEAS-2B and five lung cancer cell lines. Compared with BEAS-2B cells, KIF11 expression was significantly elevated in A549, H1299, H460, H1975, and PC9 cells (Figure 8A). Among the cancer cell lines examined, H460 cells exhibited the highest KIF11 expression, followed by H1299 cells. KIF11 expression was also increased in A549, H1975, and PC9 cells, although to varying

degrees. On the basis of their relatively high endogenous KIF11 levels, H460 and H1299 cells were selected for subsequent loss-of-function experiments.

To assess the efficiency of KIF11 silencing, H460 and H1299 cells were transfected with three independent KIF11-targeting siRNAs. Quantitative RT-PCR confirmed that all three siRNAs reduced KIF11 mRNA expression compared with the non-targeting control in both cell lines (Figure 8B, C). Based on their relatively high mRNA silencing efficiencies, si-KIF11 1# and si-KIF11 2# were selected for subsequent functional analyses and were further validated at the protein level. Western blotting confirmed that both selected siRNAs markedly reduced KIF11 protein abundance in H460 and H1299 cells compared with the corresponding si-NC groups (Supplementary Figure 1).

CCK-8 assays showed a progressive increase in viable cell accumulation over time in all experimental groups. However, KIF11-depleted H460 cells displayed lower OD450 values than si-NC-transfected cells, with a significant difference observed at 96 h after seeding (Figure 8D). A comparable reduction was observed in H1299 cells following transfection with either si-KIF11 1# or si-KIF11 2# (Figure 8E). These findings indicate that KIF11 depletion attenuated the growth of both lung cancer cell lines.

Consistent with the CCK-8 results, representative colony-formation images showed fewer and less densely distributed colonies in KIF11-silenced H460 and H1299 cells than in their corresponding control cells (Figure 8F). Representative Transwell images likewise showed an apparent reduction in the number of cells migrating through the membrane after KIF11 knockdown (Figure 8G). In the wound-healing assay, the scratched areas remained wider at 24 h in the si-KIF11 1#- and si-KIF11 2#-transfected groups than in the si-NC group, suggesting delayed wound closure following KIF11 silencing (Figure 8H).

Taken together, these results show that KIF11 depletion was accompanied by reduced proliferative, clonogenic, migratory, and wound-closure phenotypes in lung cancer cells.

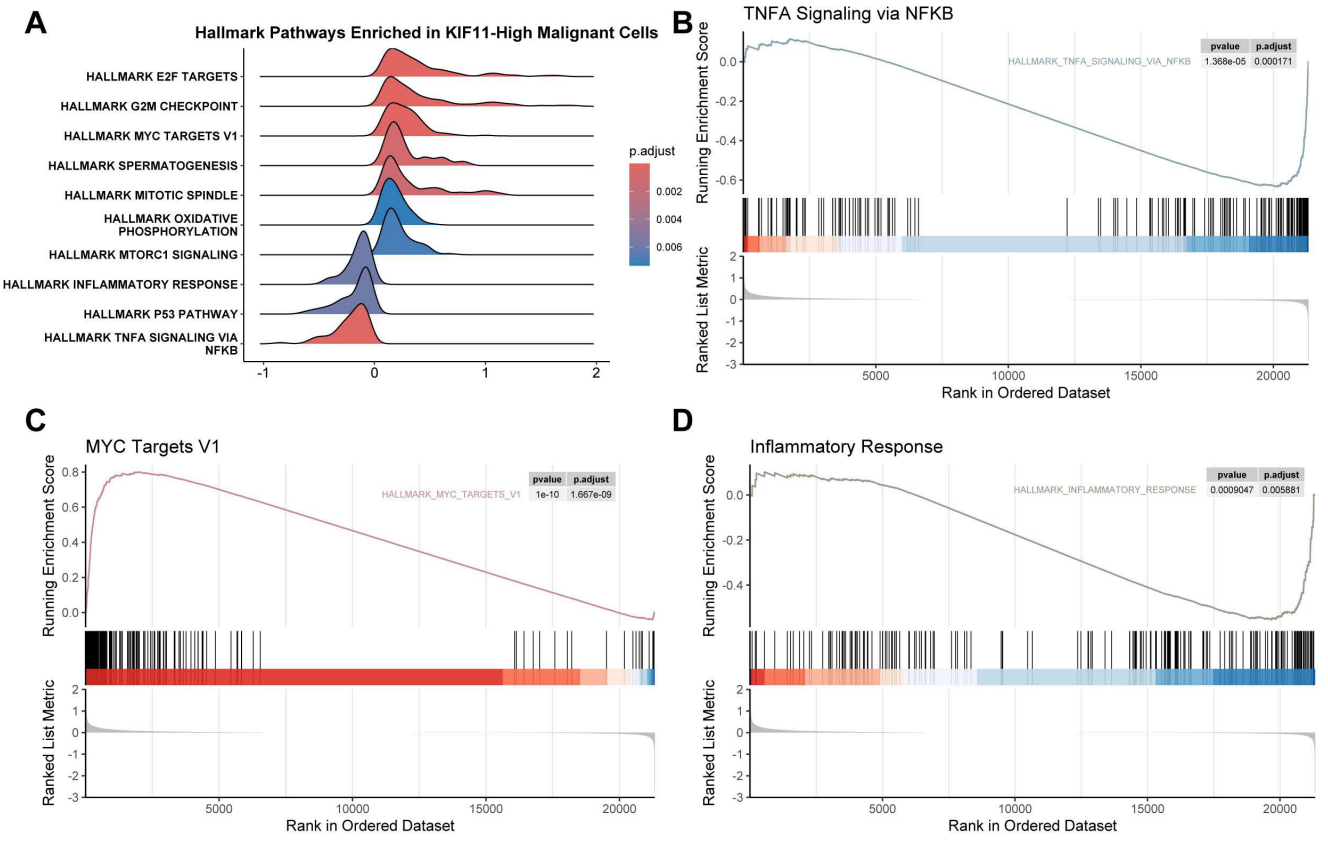


Figure 7. Pathway activity associated with KIF11 expression in malignant epithelial cells. (A) Ridge plot of Hallmark gene-set enrichment results comparing KIF11-high and KIF11-low malignant epithelial cells. (B-D) Gene set enrichment analysis plots for TNF-alpha signaling via NF-kB, MYC targets V1 and inflammatory response, respectively.

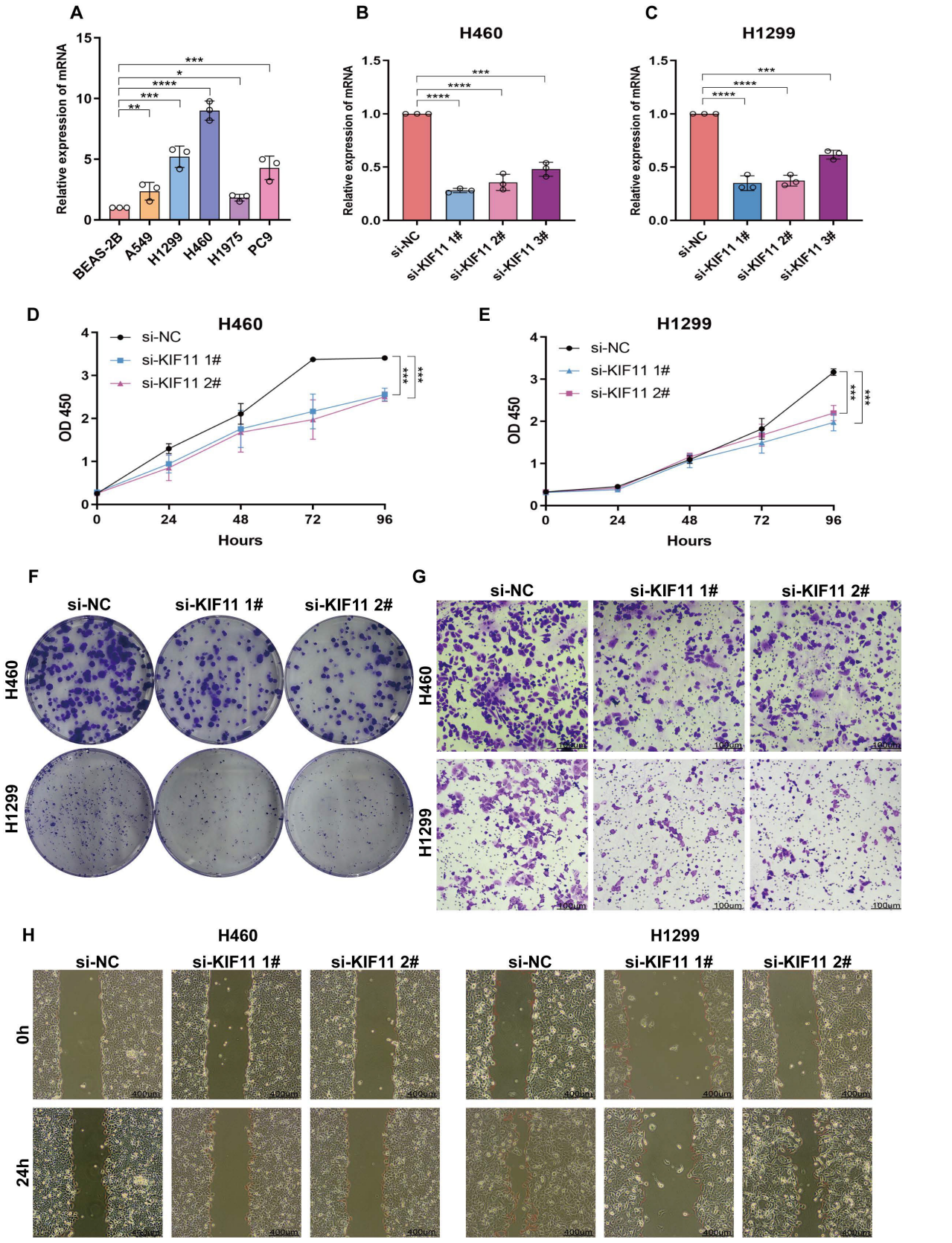


Figure 8. KIF11 knockdown attenuates proliferation and migration-related phenotypes in lung cancer cells. (A) Relative KIF11 mRNA expression in BEAS-2B cells and the indicated lung cancer cell lines. (B,C) Knockdown efficiencies of three KIF11-targeting siRNAs in H460 and H1299 cells, respectively. (D,E) CCK-8 growth curves of H460 and H1299 cells after transfection with si-NC, si-KIF11 1# and si-KIF11 2#. (F) Colony formation assays of the control and siRNA-treated groups in different cell lines. CCK-8 and colony-formation assays were independently repeated three times. Quantitative data are presented as mean ± SD from three independent experiments (n = 3). (G) Transwell assay for cell migration ability of H460 and H1299 cells after KIF11 knockdown. Scale bar = 100 μm. (H) Wound healing assay for cell migration capacity of H460 and H1299 cells after KIF11 knockdown. Scale bar = 400 μm.

Discussion

In this study, we developed and externally validated a mechanobiology-related prognostic signature for lung adenocarcinoma (LUAD), and then prioritized KIF11 as a high-risk component. Multiple lines of evidence converged on KIF11: its expression was elevated in LUAD tissues, associated with unfavorable survival and an immune-depleted phenotype, positively correlated with the prognostic risk score, and enriched in malignant epithelial cells displaying prominent cell-cycle-related transcriptional programs. KIF11, also known as Eg5 or kinesin spindle protein, is required for bipolar spindle formation; its depletion can produce monopolar spindles and mitotic arrest [22]. Thus, the enrichment of mitotic-spindle, E2F-target and G2/M-checkpoint programs in KIF11-high malignant cells provides a biologically coherent context for the prognostic association, while not by itself establishing that KIF11 is the initiating driver of these transcriptional states. The cell-based experiments add functional support to this interpretation. KIF11 silencing reduced the accumulation of viable H460 and H1299 cells, clonogenic growth, Transwell migration and wound closure. Although H460 and H1299 have been frequently employed in LUAD-focused experimental studies, their histological annotation is not uniform across cell-line resources, and H460 in particular is classically classified as a large-cell lung carcinoma model. Accordingly, the present H460/H1299 experiments should be interpreted as complementary functional validation in lung cancer cells rather than definitive LUAD-specific experimental evidence. Their selection in the present study was based on their relatively high endogenous KIF11 expression. Further validation in canonical LUAD cell lines, such as A549 and PC9, will be valuable for establishing the generalizability of these findings within LUAD. These data are consistent with a model in which KIF11 helps sustain proliferative and motile phenotypes in lung cancer cells. A previous LUAD study similarly reported that KIF11 knockdown inhibited proliferation, migration and invasion [23]. Building on their findings, our study further integrates multi-cohort prognostic modeling, immunotherapy-response analyses, and single-cell transcriptomics. Notably, we identified an association between KIF11-high malignant cells, enhanced proliferative signaling, and attenuated inflammatory pathways, providing additional insights into its potential relevance to an immune-cold tumor phenotype and immunotherapy resistance. However, the underlying causal mechanisms require further investigation. The essential mitotic role of KIF11 has also motivated pharmacological inhibition as an anticancer strategy, although current evidence does not establish clinical utility in LUAD [24]. However, the current assays are phenotypic: they do not resolve whether the migration phenotype is a direct consequence of altered microtubule mechanics, a secondary consequence of cell-cycle perturbation, or both. Cell-cycle profiling, rescue experiments and in vivo models will be required to separate these possibilities.

Another observation was the inverse association between KIF11 expression and the ESTIMATE-derived stromal, immune and composite scores, together with a positive association with estimated tumor purity. ESTIMATE uses expression signatures to infer stromal and immune admixture from bulk tumor transcriptomes [17]. The pattern is compatible with an immune-depleted or tumor-cell-dominant state. This interpretation is conceptually relevant to the mechanical framework of the signature: extracellular-matrix remodeling and stiffness can influence tumor progression, immune-cell access and immunotherapy efficacy [25]. In preclinical models, reducing collagen cross-linking and tumor stiffening improved intratumoral T-cell migration and anti-PD-1 efficacy [26]. Additional studies indicate that fibrotic, stiff microenvironments can also limit CD8-positive T-cell function through macrophage-associated metabolic programs [27]. Importantly, the present study did not directly measure tissue stiffness, extracellular-matrix architecture, or force transmission. Therefore, our data do not establish KIF11 as a sensor or mediator of extracellular mechanical cues. Rather, KIF11 should be interpreted in the present study as a mechanobiology-related intracellular microtubule motor whose established functions in microtubule sliding, spindle organization, and mitotic mechanics place it within the broader context of intracellular mechanical regulation. Future studies using tunable matrix-stiffness systems, three-dimensional culture models, and quantitative force measurements will be needed to determine whether KIF11 functionally interacts with extracellular mechanical properties in LUAD.

The ICB analyses represent a translational strength of this study. Rather than relying on a single computational predictor, we integrated three independent NSCLC-related ICB cohorts spanning anti-PD-1-treated NSCLC (GSE126044), anti-PD-1-treated LUAD (GSE166449), and neoadjuvant PD-1 blockade plus chemotherapy in resectable NSCLC (GSE207422) [12-14]. Across the integrated ICB analysis, higher KIF11 expression was associated with non-response, while the KIF11-high group also exhibited higher TIDE scores and lower immunophenoscores. The concordance between

observed response status and two complementary transcriptome-based immune-response metrics strengthens the clinical relevance of KIF11 as a candidate marker of an immune-cold, treatment-refractory phenotype [28]. Importantly, the inclusion of cohorts with distinct disease settings and treatment regimens suggests that the KIF11-associated signal may capture a biologically meaningful feature of the NSCLC immune landscape.

Single-cell RNA sequencing enables the characterization of transcriptional heterogeneity and cell-state diversity at single-cell resolution [29, 30]. Representative single-cell studies in LUAD have further revealed substantial malignant-cell heterogeneity and dynamic tumor–microenvironmental remodeling during disease progression [15, 31, 32]. These studies also provided important methodological and conceptual support for the analytical strategy adopted in the present study. The single-cell analysis provides an additional major strength by localizing the KIF11-associated phenotype to malignant epithelial cells rather than inferring it solely from bulk transcriptomic data. In the LUAD single-cell atlas, KIF11-high malignant cells showed coordinated enrichment of E2F targets, G2/M checkpoint, MYC targets V1 and mitotic-spindle programs, together with relative depletion of inflammatory-response and TNF-alpha/NF-kB signaling. This cell-resolved pattern offers a coherent link between KIF11 expression, proliferative capacity and an immune-poor transcriptional context. It also enables the present study to connect tumor-intrinsic KIF11 activity with the broader cellular microenvironment of LUAD progression.

Collectively, the principal strength of this work is its multi-level evidence framework. The mechanobiology-related prognostic signature was developed through extensive machine-learning benchmarking, externally evaluated across five independent LUAD cohorts, compared with established clinical variables and published signatures, and then refined to a biologically and clinically relevant core gene. KIF11 was subsequently supported by bulk transcriptomic associations, immune-context analyses, single-cell localization and loss-of-function experiments in two lung cancer cell lines. This convergence across population-level prognosis, tumor-microenvironment features, cell-state programs and functional phenotypes provides a strong rationale for considering KIF11 a promising prognostic biomarker and therapeutic candidate in LUAD.

Supplementary Material

Supplementary figure and table.
https://www.jcancer.org/v17p2137s1.pdf

Acknowledgements

The authors gratefully acknowledge the Gene Expression Omnibus (GEO) and The Cancer Genome Atlas (TCGA) for providing access to the data used in this study.

Funding

This study was supported by funds from the National Natural Science Foundation of China (Grant numbers: 82172835).

Availability of data and materials

The datasets analyzed in this study are publicly available in online repositories. The corresponding repository names and accession numbers are provided in the main text of the article.

Author contributions

Wenbin Jia and Zewei Zhao designed the study, conducted data collection, data processing, and statistical analysis. Jiaqi Zhou, Bowen Liu and Xinchao Li wrote the manuscript. Chunlan Ning and Yu Zou interpreted the results, conducted the experiments and revised the manuscript. Xuchen Cao, Xin Wang and Yue Yu provided overall guidance for this work. All authors have read and approved the final manuscript.

Competing Interests

The authors have declared that no competing interest exists.

References

1. Bray F, Laversanne M, Sung H, Ferlay J, Siegel RL, Soerjomataram I, et al. Global cancer statistics 2022: GLOBOCAN estimates of incidence and mortality worldwide for 36 cancers in 185 countries. CA Cancer J Clin. 2024; 74: 229-63.
2. Hendriks LEL, Remon J, Faivre-Finn C, Garassino MC, Heymach JV, Kerr KM, et al. Non-small-cell lung cancer. Nat Rev Dis Primers. 2024; 10: 71.
3. Humphrey JD, Dufresne ER, Schwartz MA. Mechanotransduction and extracellular matrix homeostasis. Nat Rev Mol Cell Biol. 2014; 15: 802-12.
4. Sleeboom JJF, van Tienderen GS, Schenke-Layland K, van der Laan LJW, Khalil AA, Verstegen MMA. The extracellular matrix as hallmark of cancer and metastasis: From biomechanics to therapeutic targets. Sci Transl Med. 2024; 16: eadg3840.
5. Sahai E, Astsaturov I, Cukierman E, DeNardo DG, Egeblad M, Evans RM, et al. A framework for advancing our understanding of cancer-associated fibroblasts. Nat Rev Cancer. 2020; 20: 174-86.
6. Thorsson V, Gibbs DL, Brown SD, Wolf D, Bortone DS, Ou Yang TH, et al. The Immune Landscape of Cancer. Immunity. 2018; 48: 812-30 e14.
7. Huse M. Mechanical forces in the immune system. Nat Rev Immunol. 2017; 17: 679-90.
8. Du H, Bartleson JM, Butenko S, Alonso V, Liu WF, Winer DA, et al. Tuning immunity through tissue mechanotransduction. Nat Rev Immunol. 2023; 23: 174-88.
9. Pavin N, Tolic IM. Mechanobiology of the Mitotic Spindle. Dev Cell. 2021; 56: 192-201.
10. Blangy A, Lane HA, d'Herin P, Harper M, Kress M, Nigg EA. Phosphorylation by p34cdc2 regulates spindle association of human Eg5, a kinesin-related motor essential for bipolar spindle formation in vivo. Cell. 1995; 83: 1159-69.
11. Kapitein LC, Peterman EJ, Kwok BH, Kim JH, Kapoor TM, Schmidt CF. The bipolar mitotic kinesin Eg5 moves on both microtubules that it crosslinks. Nature. 2005; 435: 114-8.
12. Cho JW, Hong MH, Ha SJ, Kim YJ, Cho BC, Lee I, et al. Genome-wide identification of differentially methylated promoters and enhancers associated with response to anti-PD-1 therapy in non-small cell lung cancer. Exp Mol Med. 2020; 52: 1550-63.

13. Lee JS, Nair NU, Dinstag G, Chapman L, Chung Y, Wang K, et al. Synthetic lethality-mediated precision oncology via the tumor transcriptome. Cell. 2021; 184: 2487-502 e13.
14. Hu J, Zhang L, Xia H, Yan Y, Zhu X, Sun F, et al. Tumor microenvironment remodeling after neoadjuvant immunotherapy in non-small cell lung cancer revealed by single-cell RNA sequencing. Genome Med. 2023; 15: 14.
15. Kim N, Kim HK, Lee K, Hong Y, Cho JH, Choi JW, et al. Single-cell RNA sequencing demonstrates the molecular and cellular reprogramming of metastatic lung adenocarcinoma. Nat Commun. 2020; 11: 2285.
16. Ritchie ME, Phipson B, Wu D, Hu Y, Law CW, Shi W, et al. limma powers differential expression analyses for RNA-sequencing and microarray studies. Nucleic Acids Res. 2015; 43: e47.
17. Yoshihara K, Shahmoradgoli M, Martinez E, Vegesna R, Kim H, Torres-Garcia W, et al. Inferring tumour purity and stromal and immune cell admixture from expression data. Nat Commun. 2013; 4: 2612.
18. Wu T, Hu E, Xu S, Chen M, Guo P, Dai Z, et al. clusterProfiler 4.0: A universal enrichment tool for interpreting omics data. Innovation (Camb). 2021; 2: 100141.
19. McGinnis CS, Murrow LM, Gartner ZJ. DoubletFinder: Doublet Detection in Single-Cell RNA Sequencing Data Using Artificial Nearest Neighbors. Cell Syst. 2019; 8: 329-37 e4.
20. Korsunsky I, Millard N, Fan J, Slowikowski K, Zhang F, Wei K, et al. Fast, sensitive and accurate integration of single-cell data with Harmony. Nat Methods. 2019; 16: 1289-96.
21. Hafemeister C, Satija R. Normalization and variance stabilization of single-cell RNA-seq data using regularized negative binomial regression. Genome Biol. 2019; 20: 296.
22. Rapley J, Nicolas M, Groen A, Regue L, Bertran MT, Caelles C, et al. The NIMA-family kinase Nek6 phosphorylates the kinesin Eg5 at a novel site necessary for mitotic spindle formation. J Cell Sci. 2008; 121: 3912-21.
23. Li Z, Yu B, Qi F, Li F. KIF11 Serves as an Independent Prognostic Factor and Therapeutic Target for Patients With Lung Adenocarcinoma. Front Oncol. 2021; 11: 670218.
24. Silva JPN, Silva PMA, Bousbaa H. Kinesin Spindle Protein (KIF11) in Mitosis and Cancer. Int J Mol Sci. 2025; 26.
25. Mai Z, Lin Y, Lin P, Zhao X, Cui L. Modulating extracellular matrix stiffness: a strategic approach to boost cancer immunotherapy. Cell Death Dis. 2024; 15: 307.
26. Nicolas-Boluda A, Vaquero J, Vimeux L, Guilbert T, Barrin S, Kantari-Mimoun C, et al. Tumor stiffening reversion through collagen crosslinking inhibition improves T cell migration and anti-PD-1 treatment. Elife. 2021; 10.
27. Tharp KM, Kersten K, Maller O, Timblin GA, Stashko C, Canale FP, et al. Tumor-associated macrophages restrict CD8(+) T cell function through collagen deposition and metabolic reprogramming of the breast cancer microenvironment. Nat Cancer. 2024; 5: 1045-62.
28. Jiang P, Gu S, Pan D, Fu J, Sahu A, Hu X, et al. Signatures of T cell dysfunction and exclusion predict cancer immunotherapy response. Nat Med. 2018; 24: 1550-8.
29. Zheng GX, Terry JM, Belgrader P, Ryvkin P, Bent ZW, Wilson R, et al. Massively parallel digital transcriptional profiling of single cells. Nat Commun. 2017; 8: 14049.
30. Picelli S, Bjorklund AK, Faridani OR, Sagasser S, Winberg G, Sandberg R. Smart-seq2 for sensitive full-length transcriptome profiling in single cells. Nat Methods. 2013; 10: 1096-8.
31. Wang Z, Li Z, Zhou K, Wang C, Jiang L, Zhang L, et al. Deciphering cell lineage specification of human lung adenocarcinoma with single-cell RNA sequencing. Nat Commun. 2021; 12: 6500.
32. Chen Z, Chen M, Yang C, Wang J, Gao Y, Feng Y, et al. Integration of Multi-Scale Profiling and Machine Learning Reveals the Prognostic Role of Extracellular Matrix-Related Cancer-Associated Fibroblasts in Lung Adenocarcinoma. Int J Med Sci. 2025; 22: 2956-72.